ENGINEERING

Atomic Sn–enabled high-utilization, large-capacity, and long-life Na anode

Fei Xu[1]*, Changzhen Qu[1], Qiongqiong Lu[2], Jiashen Meng[3], Xiuhai Zhang[1], Xiaosa Xu[1], Yuqian Qiu[1], Baichuan Ding[1], Jiaying Yang[1], Fengren Cao[4], Penghui Yang[1], Guangshen Jiang[1], Stefan Kaskel[5], Jingyuan Ma[6], Liang Li[4]*, Xingcai Zhang[3,7]*, Hongqiang Wang[1]*

Constructing robust nucleation sites with an ultrafine size in a confined environment is essential toward simultaneously achieving superior utilization, high capacity, and long-term durability in Na metal-based energy storage, yet remains largely unexplored. Here, we report a previously unexplored design of spatially confined atomic Sn in hollow carbon spheres for homogeneous nucleation and dendrite-free growth. The designed architecture maximizes Sn utilization, prevents agglomeration, mitigates volume variation, and allows complete alloying-dealloying with high-affinity Sn as persistent nucleation sites, contrary to conventional spatially exposed large-size ones without dealloying. Thus, conformal deposition is achieved, rendering an exceptional capacity of 16 mAh cm^{-2} in half-cells and long cycling over 7000 hours in symmetric cells. Moreover, the well-known paradox is surmounted, delivering record-high Na utilization (e.g., 85%) and large capacity (e.g., 8 mAh cm^{-2}) while maintaining extraordinary durability over 5000 hours, representing an important breakthrough for stabilizing Na anode.

INTRODUCTION

The pursuit of future energy-dense low-cost metal-based batteries (e.g., Na) has stimulated tremendous efforts in constructing robust interphases to tackle intrinsic interfacial instability, as ultimately being manifested as uncontrolled dendrite growth with serious performance deterioration (*1*–*4*). Approaches including optimizing electrolytes (*5*, *6*), constructing solid-state electrolytes (*7*, *8*), designing artificial protective layers (*9*–*11*), and engineering porous three-dimensional scaffolds (*12*–*16*) have thus been developed for various metal anodes. The resulting anodes, Na specifically, demonstrate promising potentials with mitigated dendritic growth and boosted plating/stripping stability (*4*, *12*), whereas modulation of sodiophilic nucleation sites has been recognized as one of the most underlying factors for navigating the initial Na nucleation behavior and subsequent growth. This is because conductive Na could, in principle, deposit randomly with uncontrollable dendrite and unpredictable shape. Weak sodiophilic affinity and the large size of nucleation sites pose key limitations with high nucleation barrier, large volume variation, and thus nucleation particle pulverization during cycling. This would result in low plating/stripping capacity, reduced cycling stability, and low Na utilization ratio [depth of discharge (DOD)], giving rise to huge Na source waste, limited energy density, and even safety hazards (*17*–*19*). Therefore, exploring rational strategies of engineering sodiophilic nucleation site to circumvent the imperative hurdles of Na anode is thus highly desirable.

Recent tremendous efforts have thus been devoted to constructing nucleation sites with high sodiophilic capability, such as N, O, and S heteroatoms doping in carbons (*13*–*15*, *20*–*22*). Meanwhile, integration of sodiophilic alloys [e.g., Au (*23*, *24*), Mg (*25*), Zn (*26*), Sn (*16*, *18*, *24*, *27*), Sb (*24*, *28*), Bi (*29*), etc. (*19*, *30*)] or compounds (*31*, *32*) manifests prominent potential for stabilizing Na metal due to their facile alloying/dealloying capability and/or high-affinity with Na, similar to that for Li stabilization (*33*–*35*). The cycling life can be extended to more than 2000 hours, while most of these stabilities have been obtained at restricted capacity (≤2 mAh cm^{-2}), or vice versa (*25*). Besides, the improved durability or capacity is always at the cost of DOD [e.g., 16.7% (*25*, *36*) or 25% (*26*, *28*)]. The low DOD (<30%) is actually ubiquitous in the area for Na metal anode, a pivotal yet largely ignored issue for practical applications (*20*, *21*, *37*). One of the essential reasons for the above paradox is the large volume variation involved in the alloying/dealloying process, resulting in the nucleation site pulverization and thus the interphase decay on cycling, particularly for those large-size ones (*24*, *27*). Downsizing sodiophilic nucleation sites helps to mitigate the volume variation and guarantee interphase stability for improved performances, such as a DOD of up to 67%, a capacity of 4 mAh cm^{-2}, and prolonged cycling (≤1600 hours) (*17*, *18*). However, these reduced nucleation sites were usually supported on exposed surfaces and sometimes with self-agglomeration, giving rise to nonuniform nucleation with dendrite growth. Control over the cutoff stripping potential without dealloying can ease volume variation (*24*). However, a vast amount of Na is irreversibly consumed initially, and as-formed Na-metal alloys essentially function as nucleation sites, which could decrease the sodiophilic affinity (*23*). We envision that the ideal structure of a nucleation site should be designed in such a fashion: further downsizing dimensions even to atomic levels while confining in a spatial nanospace to permit complete alloy-dealloying. In this circumstance, current uncharted performance terrain toward achieving remarkable DOD (e.g., ≥80%) while synchronously maintaining

[1]State Key Laboratory of Solidification Processing, Center for Nano Energy Materials, School of Materials Science and Engineering, Northwestern Polytechnical University and Shaanxi Joint Laboratory of Graphene (NPU), Xi'an 710072, P. R. China. [2]Leibniz Institute for Solid State and Materials Research (IFW) Dresden e.V. Helmholtzstr 20, Dresden 01069, Germany. [3]School of Engineering, Massachusetts Institute of Technology, Cambridge, MA 02139, USA. [4]School of Physical Science and Technology, Jiangsu Key Laboratory of Thin Films, Center for Energy Conversion Materials and Physics (CECMP), Soochow University, Suzhou 215006, P. R. China. [5]Department of Inorganic Chemistry, Technische Universität Dresden, Bergstrasse 66, Dresden 01062, Germany. [6]Shanghai Synchrotron Radiation Facility, Shanghai Advanced Research Institute, Chinese Academy of Sciences, Shanghai 201204, P. R. China. [7]John A. Paulson School of Engineering and Applied Sciences, Harvard University, Cambridge, MA 02138, USA.
*Corresponding author. Email: feixu@nwpu.edu.cn (F.X.); xingcai@mit.edu (Xingcai Zhang); lli@suda.edu.cn (L.L.) hongqiang.wang@nwpu.edu.cn (H.W.)

large areal capacities (e.g., ≥4 mAh cm^{-2}) and long-term durability over 2000 hours could be conquered, whereas investigations judiciously orchestrating such architectures have been scarcely explored.

Here, we propose a facile design of spatially confined atomic Sn in hollow carbon nanospheres (At-Sn@HCN) as a robust nucleation site for homogeneous nucleation and dendrite-free growth. At-Sn@HCN is prepared via one-pot aqueous micelle-interfacial copolymerization followed by in situ carbothermal reduction, bypassing the complicated template-assisted etching approach (*17*, *38*–*41*). The well-dispersed atomic Sn maximizes Sn utilization as a nucleation site, while micropore confinement alleviates volume variation and agglomeration, and thus reversible and complete alloying-dealloying can be achieved. Therefore, superior capacity of 16 mAh cm^{-2} is realized for 4000 hours with stable Coulombic efficiency in the half-cell, and the symmetrical cells demonstrate ultralong stability over 7000 hours. More encouragingly, the well-known paradox among the DOD, areal capacity, and durability is surmounted, delivering excellent DOD and areal capacity up to 85% at 3.4 mAh cm^{-2} and 80% at 8 mAh cm^{-2}, respectively, with extraordinary cycling over 5000 hours, which have rarely been achieved. Full cells with high-loading cathode and limited excess of Na anode also demonstrate improved stability, heralding a new paradigm for dendrite-free Na anode.

RESULTS

Design and structure of At-Sn@HCN

The synthesis schematic for At-Sn@HCN is shown in Fig. 1A. Hollow poly(aniline-co-pyrrole) spheres with SnO_2 (PACP/SnO_2) are obtained through micelle-interfacial copolymerization in the presence of SnO_2 colloids, followed by carbonization. Unless specified, the SnO_2 dosage is 2.5 ml (5.5 mM) in the following. Copolymerization at the micelle interface has been well explored in our previous work to build hollow carbon nanospheres (HCNs) and their hybrids with encapsulated particles inside a hollow cavity (*42*–*44*). Here, atomic Sn is incorporated in shell nanopores and thus is able to achieve ultimate atom utilization with a stable structure (*40*, *45*). Such versatile strategy is in sharp contrast to the template-assisted etching or post-loading pathways (fig. S1 and table S1), which are hindered by tedious multistep procedures with high cost (*17*, *38*–*41*).

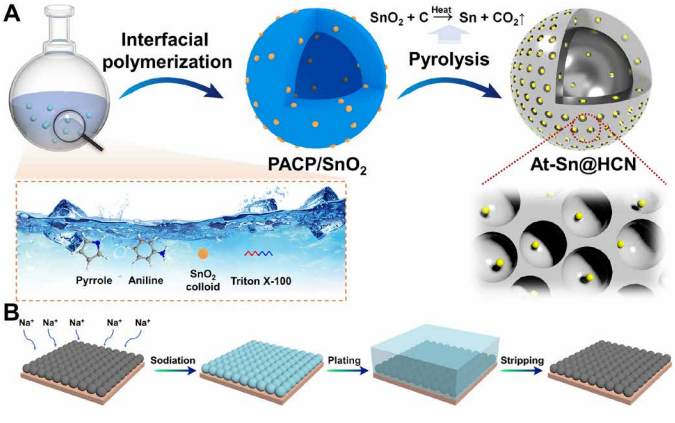

Fig. 1. Schematic diagram of the preparation and application of At-Sn@HCN in Na metal stabilization. (**A**) Fabrication procedure of At-Sn@HCN. (**B**) At-Sn@HCN as nucleation interphase for homogeneous Na nucleation and reversible plating/stripping.

PACP/SnO_2 shows uniform spherical morphology without observable SnO_2 aggregation (fig. S2), while transmission electron microscopy (TEM) image reveals the presence of hollow cores with SnO_2 on the shell (fig. S3). These results suggest that the SnO_2 presence does not interrupt the interfacial copolymerization for hollow structure formation, which otherwise does not trigger SnO_2 aggregation, whereas the use of large-size SnO_2 particles gives rise to the ill-defined spherical structure (fig. S4). After pyrolysis under 700°C, the PACP is transformed into HCN with the creation of micropores within carbon shell (*42*, *46*), while SnO_2 undergoes in situ reduction to Sn via carbothermal reaction. As shown in Fig. 2A and fig. S5, the hollow spherical morphology well remains coupled with a decrease in diameter (135 nm), smaller than those fabricated by the template-assisted etching approach (usually ≥150 nm; table S1). The spherical size can be further reduced to around 101 nm by decreasing the monomer concentration (fig. S6), while an extensive increase in SnO_2 colloids in the micelle solution (e.g., 10 ml, Ex-Sn/HCN) will result in failure in the formation of spherical morphology, together with the presence of large-size Sn particles outside (fig. S7).

It is envisioned that at 700°C, in situ reduced molten Sn keeps an intimate contact with the carbon skeleton and thus is expected to readily infiltrate the shell micropores facilitated by the capillary effect. As shown by in situ TEM images, SnO_2 nanoparticles are observed at 300°C but disappear at 600°C (fig. S8), reflecting the infiltration of in situ reduced Sn. It is found that the specific Brunauer-Emmett-Teller (BET) surface area and micropore volume of At-Sn@HCN (231 $m^2 g^{-1}$ and 0.108 $cm^3 g^{-1}$) decrease, as compared with that of HCN (331 $m^2 g^{-1}$ and 0.125 $cm^3 g^{-1}$) (fig. S9 and table S2), indicative of the micropore confinement. Furthermore, no observable Sn particles or clusters were present in high-resolution TEM images (Fig. 2B), and diffraction peaks ascribing to metallic Sn were not observed as well in the X-ray diffraction pattern (XRD, Fig. 2C), further confirming the micropore confinement of Sn, while the Ex-Sn/HCN with bulk Sn outside shows notable metallic Sn peaks (Fig. 2C). Elemental mappings vividly showcase the homogeneous distribution of Sn in the shell of At-Sn@HCN (Fig. 2B), and numerous fine and bright dots are uniformly rooted in the carbon shell with a small size, as shown in high-angle annular dark field (HAADF)–scanning transmission electron microscopy (STEM) images (Fig. 2, D and E), confirming the presence of isolated Sn atoms. The weight percentage of Sn is 10.2 wt% via Thermogravimetric (TG) analysis. Further increasing the SnO_2 dosage leads to enhanced Sn content and reduced BET surface area and micropore volume (figs. S10 and S11), revealing the gradual nanopore filling. Together, these results verified that Sn mainly existed inside micropores of At-Sn@HCN with an atomically dispersed state.

The isolated atomic feature of Sn was further validated by the X-ray absorption near-edge structure (XANES) and extended X-ray absorption fine structure (EXAFS) spectra (Fig. 2, F and G). The absorption edge in the XANES spectrum of At-Sn@HCN shifts to the higher-energy region and shows higher intensity, as compared with that of Sn foil (Fig. 2F), revealing the oxidized valence state of metal atoms (*39*, *45*). Moreover, the Fourier-transformed EXAFS spectrum exhibits a notable Sn—N coordination peak (≈1.53 Å), while the Sn—Sn peak (≈2.82 Å) largely disappears (Fig. 2G), clarifying that the Sn sites exist as an atomically dispersed state in the shell. The EXAFS results are further fitted to provide the pentagonal architecture of Sn-N5 coordination configuration (fig. S12 and table S3), in accordance with the previous report (*47*). The bonding

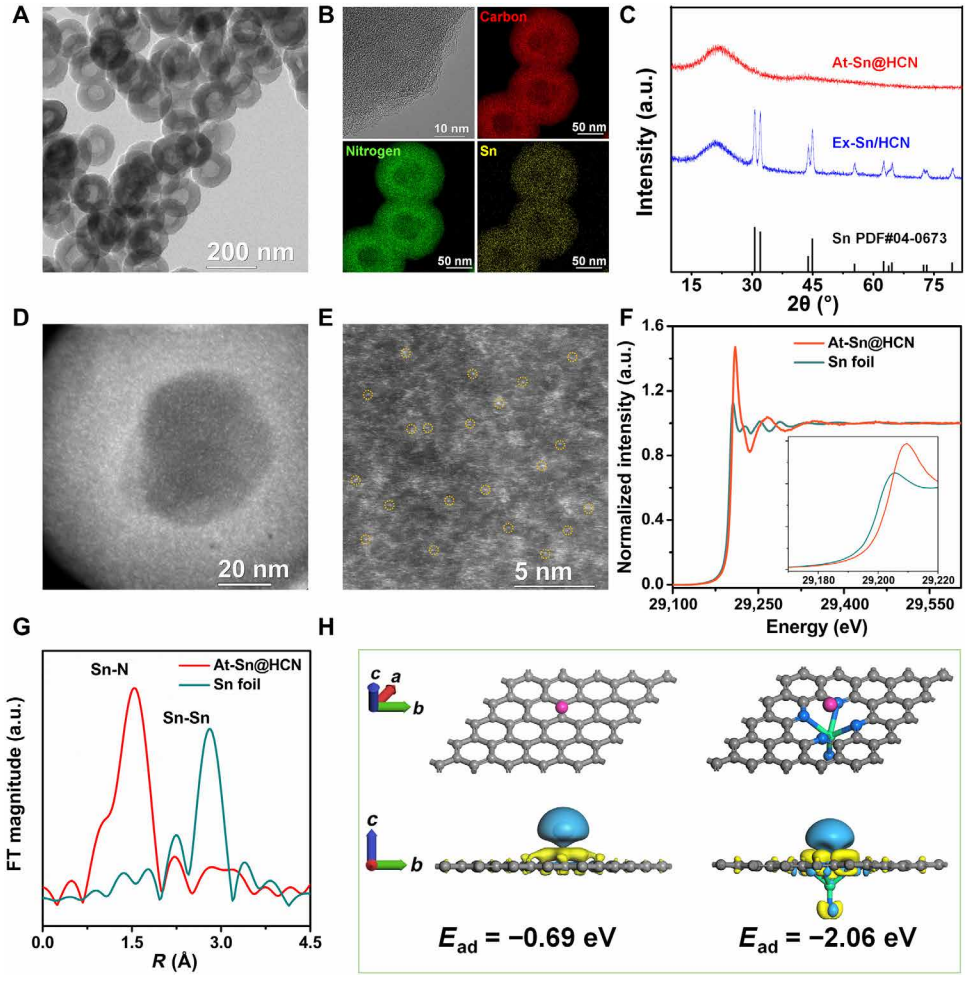

Fig. 2. Structural characterizations of At-Sn@HCN. (**A** and **B**) TEM images and corresponding elemental mappings of At-Sn@HCN. (**C**) XRD patterns of At-Sn@HCN and Ex-Sn/HCN. (**D** and **E**) HAADF-STEM images of At-Sn@HCN. Sn K-edge (**F**) XANES spectra and (**G**) Fourier-transformed EXAFS spectra of At-Sn@HCN and Sn foil. (**H**) Optimized structures and charge density difference plots of Na atom adsorption on HCN (left) and At-Sn@HCN (right).

N was confirmed by X-ray photoelectron spectroscopy (fig. S13), derived from the N-containing PACP (*42*, *48*), in which pyridinic N can serve as an anchor site for Sn coordination. It is difficult to remove atomic Sn completely by etching with HCl (fig. S14), which also reveals the coordination effect. All these results demonstrate the nanoconfinement of Sn atoms with a strong chemical coupling and micropore confinement between Sn and N-doped carbon shell.

Reversible and long-term plating/stripping

Encouraged by the unique nanoarchitecture of spatially confined atomic Sn and the synthetic simplicity, the Na metal anode performances were evaluated by using At-Sn@HCN as a nucleation buffer layer. Sodiophobic carbon frameworks are thermodynamically unfavorable for Na nucleation, exacerbating the dendrite growth, while Sn can undergo facile alloying-dealloying reactions with Na and thus serves as a preferential nucleation site (*16*, *18*, *24*). As calculated by the density functional theory (DFT) simulation, the adsorption energy (E_{ad}) of a Na atom on an ideal graphene is −0.69 eV, while the value of coordinated Sn on graphene is −2.06 eV (Fig. 2H), demonstrating much higher sodiophilicity and therefore is much more conducive to the adsorption of Na ion flux.

The enhanced binding energy would enable a lower Na nucleation barrier, as demonstrated by the nucleation overpotentials (Fig. 3A). The overpotential is only 5 mV for At-Sn@HCN at 2 mA cm^{-2}, much lower than that of HCN (12 mV) and bare Cu (54 mV; fig. S15). By increasing the current density, At-Sn@HCN always retains constantly lowest overpotentials among the HCN and bare Cu (Fig. 3B and fig. S15), such as 4 mV at 1 mA cm^{-2} and 11 mV at 4 mA cm^{-2}. These values are also lower than the previously reported Na anode under similar current densities (table S4), such as Sn/C (15.5 mV at 3 mA cm^{-2}) (*18*), Sn@C composite (~18 mV at 2 mA cm^{-2}) (*27*), Sn and Sb film (12 mV at 4 mA cm^{-2}) (*24*), Bi⊂CNs (7.4 mV at 1 mA cm^{-2}) (*29*), C-NTO-3 (10.5 mV at 3 mA cm^{-2}) (*32*), CT-Sn(II)@Ti_3C_2 (40 mV at 4 mA cm^{-2}) (*30*), h-Ti_3C_2/CNTs (6 mV at 1 mA cm^{-2}) (*49*), N, S codoped hollow carbon fibers (16.4 mV at 4 mA cm^{-2}) (*20*), and O-CCF (9 mV at 1 mA cm^{-2}) (*14*). It can thus be concluded that incorporation of high sodiophilic Sn helps to overcome the heterogeneous nucleation barrier.

The Na plating/stripping reversibility can be reflected by the Coulombic efficiency (CE), which is calculated by the ratio of stripping capacity to plating capacity. A fixed capacity was first electrochemically plated and then stripped away to 1 V. At-Sn@HCN

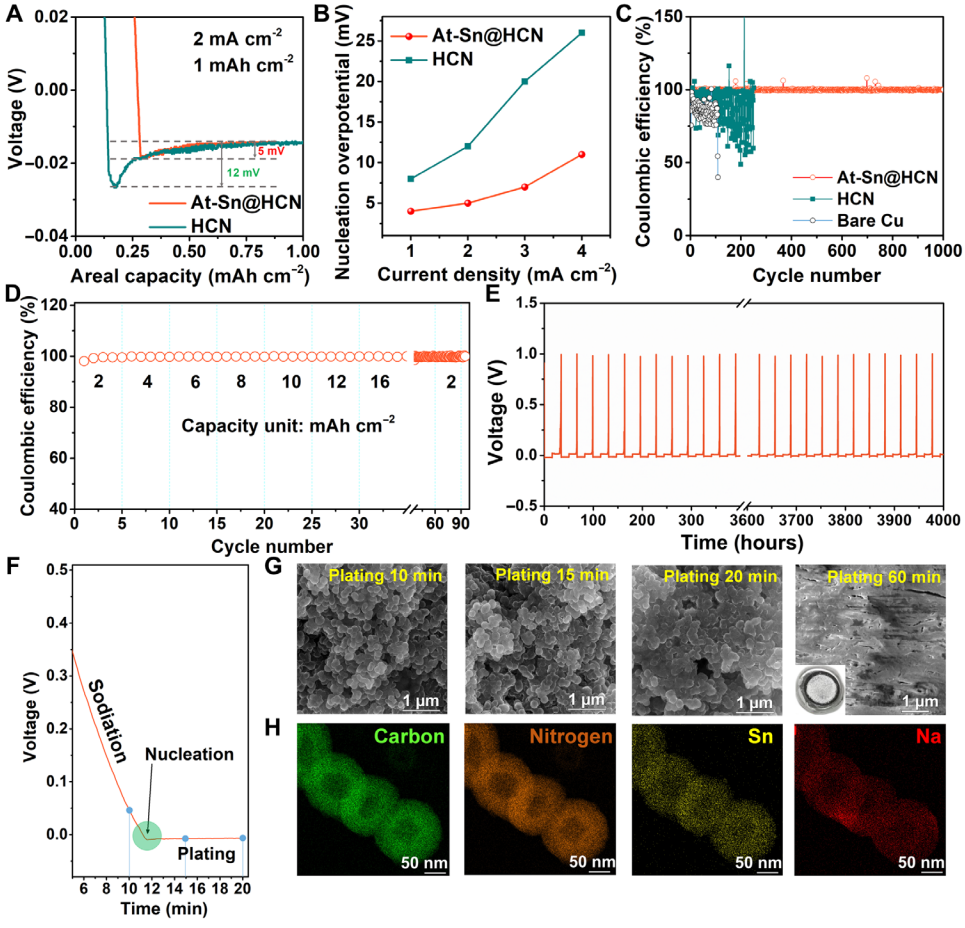

Fig. 3. Electrochemical and structural analysis in half-cells. (**A**) Voltage profiles and (**B**) nucleation overpotentials of Na deposition on the At-Sn@HCN and HCN electrode. (**C**) Coulombic efficiencies of Na plating/stripping on At-Sn@HCN, HCN, and bare Cu at 2 mA cm^{-2} and 1 mAh cm^{-2}. (**D**) Stepwise increasing the areal capacity of At-Sn@HCN from 2 to 16 mAh cm^{-2} and back to 2 mAh cm^{-2} at 1 mA cm^{-2}. (**E**) Plating/stripping curves of At-Sn@HCN at 1 mA cm^{-2} and 16 mAh cm^{-2}. (**F**) Discharging curve at the first cycle for At-Sn@HCN in half-cell at 1 mA cm^{-2}. (**G**) Corresponding SEM images after discharging for a given time. The inset is a digital photo for plating of 60 min. (**H**) Element mappings of the At-Sn@HCN electrode at the nucleation point (12 min) in (F).

delivers a high and stable CE with an average value of up to 99.93% over 1000 cycles at 1 mAh cm^{-2} and 2 mA cm^{-2} (Fig. 3C). By contrast, the HCN and bare Cu foil show fluctuating CEs with a lower average value of 90 and 86% after only 250 and 100 cycles, respectively (Fig. 3C), reflecting the repetitive growth and dissolution of Na dendrites with "dead Na." This is mainly because of the absence of preferential nucleation sites with uncontrollable deposition. The corresponding voltage-capacity profiles are provided in figs. S16 and S17, where At-Sn@HCN delivers almost overlapped profiles with negligible capacity loss and low-voltage hysteresis. Decreasing Sn content in HCN (e.g., 0.5 ml of SnO_2 dosage) would give rise to insufficient alloying nucleation site and thus leads to a slight increase in nucleation overpotential and a decrease in average CE (fig. S18). Higher current density usually gives rise to the increased probability of dendrite formation and thus is detrimental to high CE. Nevertheless, at 4 mA cm^{-2}, the average CE of 99.95% can be obtained with 500 cycles. Meanwhile, as the capacity increases to 6 mAh cm^{-2}, the CE of At-Sn@HCN is still stable around 99.96% (fig. S19). The encouraging performances inspire us to further explore the maximum plating capacity. By exerting a stepwise increased capacity even to 16 mAh cm^{-2}, the CE can steadily persist for nearly 99.90% (Fig. 3D) and can be largely recovered (99.81%) by switching back to 2 mAh cm^{-2}. Notably, At-Sn@HCN still delivers intriguing cyclability under a capacity of 16 mAh cm^{-2} with a stable average CE for 4000 hours (Fig. 3E).

Driven by the impressive reversibility and high capacity, the Na nucleation and spatial growth behavior were traced by the ex situ scanning electron microscopy (SEM) images (Fig. 3G and fig. S20). As marked in the discharge curve (Fig. 3F), the process undergoes sodiation, alloying, and deposition. At the beginning with a capacity of 0.17 mAh cm^{-2} (10 min), sodiation of carbon and alloying with Sn occur; thus, the nanospherical morphology remains, similar to the pristine one (fig. S21). With continuous discharging below 0 V, the nucleated Na metal starts to grow. As revealed by the TEM and corresponding mappings at this point (12 min), uniformly distributed Na and Sn are observed in the carbon shell without isolated bulk Na out of spheres (Fig. 3H and fig. S22). The results indicate the successful mediation of Na plating at the nucleation stage. Subsequently, Na begins to deposit by gradual filling of the nanospace between spheres (15 and 20 min, Fig. 3H), and thus, the overall electrode thickness remains unchanged during this period (fig. S23). Therefore, a lateral plating behavior is inferred to occur, in which

newly plated Na spreads into inter-sphere space with the growing direction almost parallel to electrode surface. This contrasts with the conventional Na dendrite formation in a vertical direction. With further deposition to 1 mAh cm^{-2} (60 min), a uniform layer of Na covers the At-Sn@HCN surface (Fig. 3G and its inset photo). Smooth and dendrite-free morphology was still observed even with plating up to 16 mAh cm^{-2}, as shown in the top-view SEM image in fig. S24A. From the cross-sectional SEM images in fig. S25, the thickness variation from 1 to 16 mAh cm^{-2} plating is very close to the theoretical calculated value, further corroborating the dendrite-free growth enabled by the At-Sn@HCN nucleation layer. Then, after fully stripping away, the spherical morphology reappears with few traces of metallic Na left (fig. S24B). In addition, atomic Sn in HCN is quite robust, as shown in the TEM and HAADF-STEM images with homogeneously distributed Sn after 100 cycles (fig. S26). In comparison, uneven Na grains deposit on bare Cu and then coalesced into a loose Na layer with notable protuberance upon increasing plating capacity (fig. S20). This nonuniform nucleation exaggerates the uneven electric field distribution, further facilitating nonuniform morphology, e.g., 16 mAh cm^{-2}, and residual dead Na is detected after stripping (fig. S24, C and D). The schematic illustration for plating and stripping of At-Sn@HCN and bare Cu is provided in Fig. 1B and fig. S27. All these results confirm that At-Sn@HCN nucleation architecture is conducive to Na dendrite inhibition and permits reversible plating/stripping with near-unity CE and robust cycling stability.

High interfacial stability with long-term cycling

The long-term interfacial stability was tested in symmetrical cells via galvanostatic cycling. Figure 4A displays the voltage-time profiles under a fixed capacity of 1 mAh cm^{-2} (predeposition: 4 mAh cm^{-2}) at 1 mA cm^{-2}. The At-Sn@HCN/Na symmetric cell shows a low overpotential (~3.4 mV) and remains constant for more than 4000 hours of cycling, as virtually revealed by the flat voltage plateaus (inset of

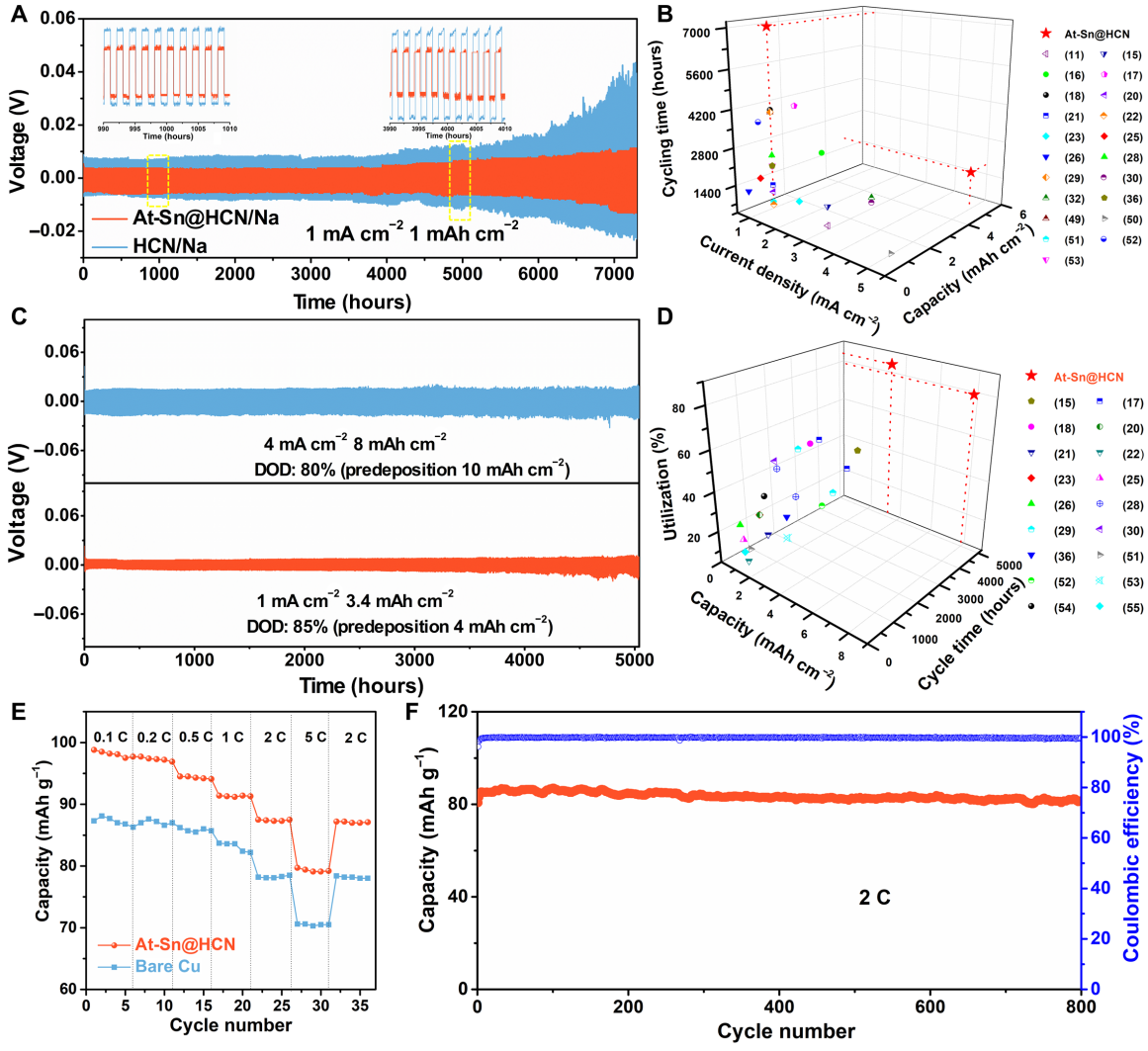

Fig. 4. Symmetric and full cell performances. (**A**) Voltage-time profiles of At-Sn@HCN and HCN in symmetric cells at an areal capacity of 1 mAh cm^{-2} and a current density of 1 mA cm^{-2}; insets show the enlarged curves around 1000 and 4000 hours. (**B**) The comparison of cycle stability, current density, and areal capacity with previous works. (**C**) Voltage-time profiles of At-Sn@HCN in symmetric cells with DODs of 80 and 85%. (**D**) The comparison of DOD, capacity, and cycle life with previous literatures. (**E**) The rate test from 0.1 to 5 C and back to 2 C for At-Sn@HCN/Na||NVP and Cu/Na||NVP full cells. (**F**) Long-term cycling of At-Sn@HCN/Na||NVP full cell at 2 C.

Fig. 4A). The overpotential increases to around 9 mV with cycling even at an unprecedented 7000 hours. Such slight increase with fluctuation especially after 4000 hours probably due to the side reactions gradually accumulated during the long-term cycling. In contrast, the voltage profiles of the HCN/Na symmetric cell display higher overpotentials with uneven rising and falling, particularly notable after 4000 cycles (e.g., 37 mV for 7000 hours). The superiority of At-Sn@HCN is more obvious at a higher current density of 5 mA cm^{-2} and a capacity of 5 mAh cm^{-2} (fig. S28). Most of the reported durability for Na anode is limited to 2000 hours with a few around 4000 hours (*13*, *17*, *18*). Our unprecedented long-term cycling of 7000 hours is thus a record value (Fig. 4B and table S5). Electrochemical impedance spectroscopy (EIS) shows that the resistance is quite low and stable after 50 and 300 cycles for At-Sn@HCN/Na (around 6.0 Ohm), while HCN/Na delivers a large resistance of about 50.0 Ohm after 300 cycles (fig. S29).

Ultrahigh Na utilization

The plating/stripping interfacial stability related to not only the current density and areal capacity but also the Na metal utilization ratio, i.e., DOD, which is also an important indicator but unfortunately quite low in previous studies (<30%), causing huge Na source waste, low energy density, and severe safety hazards (*17*, *18*). Recent endeavors show some progress in enhancing DOD but at the cost of cycle life and capacity such as a DOD of 67% with a limited cycle life of 1600 hours for C@Ag (*17*), 1275 hours for Sn/C (*18*), and 850 hours for Bi/C (*29*). Consequently, achieving long-term durability under high DOD and large capacity remains challenging. Intriguingly, the At-Sn@HCN/Na symmetric cell can be steadily cycled with a DOD of up to 80% at a capacity of 8 mAh cm^{-2} over 5000 hours, a record-high value as far as we know (Fig. 4C). Furthermore, an unprecedented DOD of up to 85% was realized for cycling over 5000 hours at 3.4 mAh cm^{-2}. Recent reported literatures with corresponding DOD, cycling time, and areal capacity were summarized (Fig. 4D and table S6) for a better proof of superior performances of At-Sn@HCN. Undoubtedly, our strategy of introducing atomic Sn in HCN thus suggests a new benchmark for Na metal anode.

Proof-of-concept full cells were assembled with $Na_3V_2(PO_4)_3$ (NVP) as cathode for evaluating potential applications. An initial discharge capacity of 94.7 mAh g^{-1} was achieved at 0.5 C, and the capacity retention ratio of 90% remains over 200 cycles for the At-Sn@HCN/Na anode, whereas full cells using the bare Cu/Na anode show decreased initial capacity and fail at the 76th cycle (fig. S30), mainly due to the short circuit with dendrite formation. The rate performance is also superior to the bare Cu/Na-based full cell (Fig. 4E), exhibiting reversible capacities of 97.7, 96.9, 94.1, 91.3, 87.5, and 79.2 mAh g^{-1} as the current density increases from 0.1 to 5 C. After switching back to 2 C, the cell still reveals a high capacity of 87.1 mAh g^{-1}. The corresponding charge and discharge plateaus are evident, and the polarization increases slightly with the rate increment (fig. S31A). More intriguingly, the long-term durability under 2 C was also measured, delivering an outstanding cycling stability and an average CE of 99.73% for 800 cycles (Fig. 4F), as also shown by the small and stable polarization between the charge and discharge plateaus (fig. S31B). Considering practical implementation, it is necessary to use a high areal cathode capacity and limited Na metal, namely, low negative to positive electrode capacity (N/P < 2), but it is largely neglected in previous work (table S7). Thus, harsh conditions were explored with cathode mass loading up to 7 mg cm^{-2} and N/P down to 1.2 (fig. S31C). In this context, the At-Sn@HCN/Na||NVP cell exhibits specific capacities of 81.4 mAh g^{-1} after 100 cycles with a capacity retention of up to 93.0%, offering promising opportunities to accelerate the practical adoption of Na metal anodes.

DISCUSSION

Underlying role of confined atomic Sn

Control experiments with excess Sn outside HCN and large-size Sn microparticles were also measured to reveal the essential role of Sn in atomically dispersed, micropore-confined configuration (figs. S7 and S32). Sn microparticles exhibit two couples of peaks in cyclic voltammetry (CV) curves (Fig. 5A), mainly due to the multistep alloying/dealloying reactions between Sn and terminal equilibrium $Na_{15}Sn_4$ (*18*, *24*, *27*), while At-Sn@HCN shows only a broad quasi-rectangular curve, probably due to the low content of Sn (fig. S33). The alloying capability of Sn upon sodiation could serve as a preferential nucleation seed based on the Na-Sn binary phase diagram (fig. S34). For the sodiation of atomic Sn, the EXAFS of the At-Sn@HCN electrode after discharging to 0.01 V was measured, and the results show the remaining of the atomic Sn and the occurrence of sodiation reaction, but probably in a different manner with large-size Sn (fig. S35). In-depth sodiation reaction of atomic Sn is worthy of further investigation. Typical alloying/dealloying involves large volume variations and thus suffers from particle pulverization, which is detrimental to long-term durability (*18*, *24*). This can be revealed by the irregular CE fluctuation after 600 cycles for Ex-Sn/HCN under the same conditions (fig. S36), in contrast to At-Sn@HCN.

To avoid such pulverization, the current strategy is to avoid the dealloying, such as control over the cutoff stripping potential. As an example of a Sn microparticle, when fixing the cutoff potential at 0.1 V, realloying is suppressed, and the half-cell can be cycled with stable CE close to 99.73% except the first cycle (fig. S37). However, with plating to 1 V like that for At-Sn@HCN, the Sn microparticle undergoes stepwise dealloying but overcharges at 0.54 V (Fig. 5D), causing the failure of the half-cell due to the irreversible side reactions. However, there are some drawbacks in using the cutoff potential: (i) Plenty of Na is irreversibly consumed in the first plating procedure, as reflected by the low CE in the first cycle for both the Sn microparticle (31.75%) and At-Sn@HCN (68.13%) (the inset of Fig. 5D); (ii) in this context, Na cycling proceeded using the irreversibly formed Na-Sn alloy (e.g., $Na_{15}Sn_4$) as a nucleation site after the first cycle. Currently, the sodiophilic nature of alloying species, for example, whether metal or its Na-metal alloy interphase has better affinity, has remained unexplored. Therefore, Na affinity toward Sn and $Na_{15}Sn_4$ alloy (upon cutoff potential of 0.1 V) was evaluated using DFT calculations. The E_{ad} of an isolated Na atom on Sn is notably lower than that of $Na_{15}Sn_4$, indicative of higher sodiophilicity for Sn (Fig. 5, B and C). In our design, downsizing of Sn to an atomic-dispersed state while confined inside micropores can effectively mitigate the volume change and stabilize the interphase even with complete dealloying during each cycle. Thus, much higher sodiophilic Sn with higher affinity persistently acts as a nucleation site. These structural advantages are displayed in Fig. 5E, which are together responsible for the ultralong durability with record-high Na utilization and large areal capacities. An ongoing effort aims to further reduce the nucleation layer loading to suppress any undesirable side reaction and enhance the overall energy density of cell in view of practical applications.

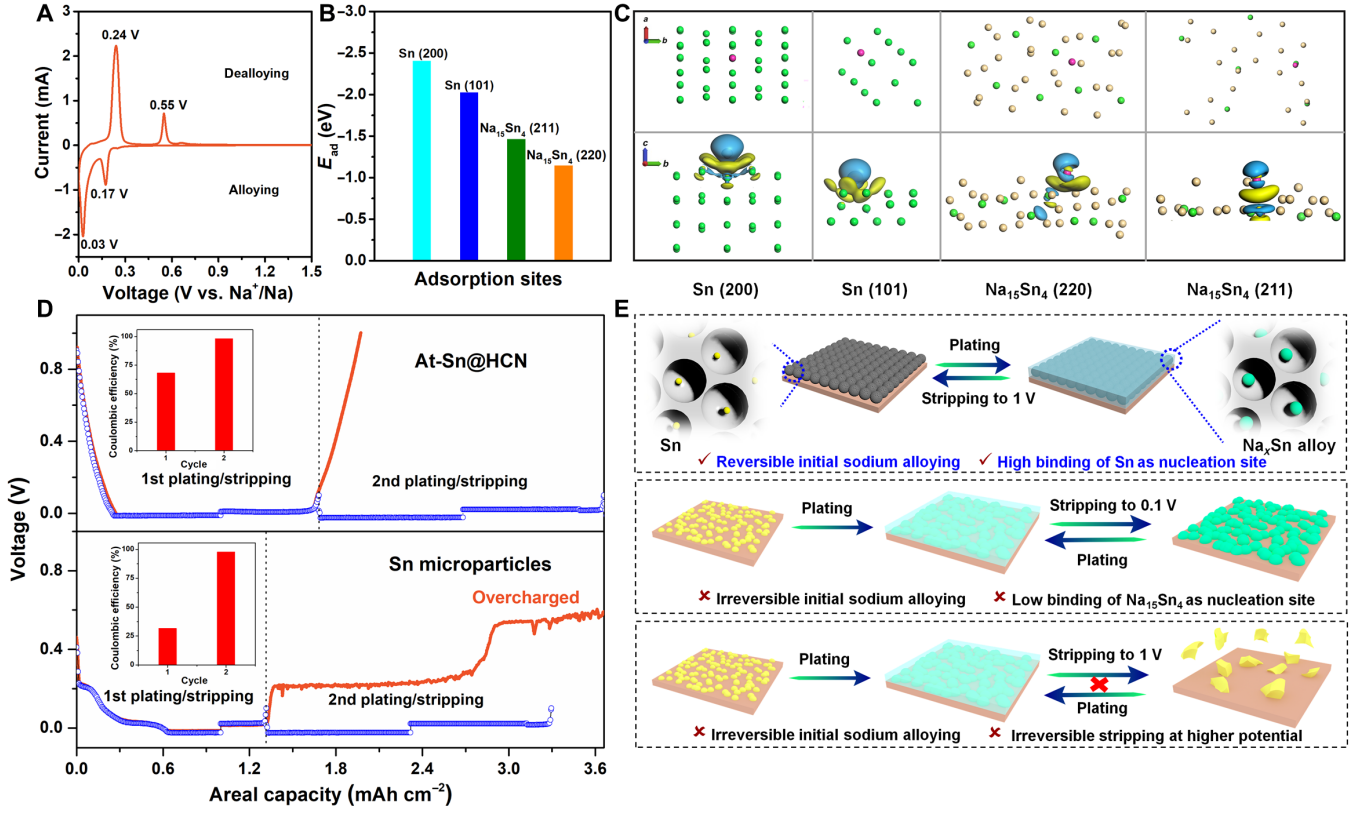

Fig. 5. Mechanism analysis of atomic Sn nucleation sites. (**A**) The CV curve of the Sn microparticle electrode at 0.1 mV s^{-1}. (**B**) Adsorption energy between different lattice planes of Sn and $Na_{15}Sn_4$ and (**C**) the corresponding optimized structures and charge density difference plots of Na atom adsorption. (**D**) Voltage capacity profiles of At-Sn@HCN and Sn microparticle electrode under different cutoff potentials of 1 and 0.1 V at 2 mA cm^{-2} and 1 mAh cm^{-2}. (**E**) Schematic illustration of plating/stripping behaviors for At-Sn@HCN and a large-size Sn system.

To summarize, we reported the design and implementation of micropore-confined, atomic Sn in hollow carbon spheres as a robust nucleation layer for stable Na metal anode. The facile micelle-interfacial copolymerization with subsequent carbothermal reduction for At-Sn@HCN circumvents the limitations of template-assisted procedures. Such nanoarchitecture maximizes the utilization of Sn as active nucleation sites, alleviates volume variation, suppresses pulverization, and permits complete alloying-dealloying without controlling cutoff potential. Consequently, the high-affinity Sn persistently functions as a robust nucleation site, contrary to conventional spatially exposed aggregated ones. Therefore, an extraordinary capacity and ultralong cycling are realized, and the well-known paradox among Na utilization, areal capacity, and durability is surmounted. Such elaborate architectural design and excellent performances offer an impetus for dendrite-free metal batteries.

MATERIALS AND METHODS

Materials synthesis

SnO_2 colloid was obtained by a modified sol-gel method. Specifically, $SnCl_2{\cdot}2H_2O$ (0.9 g) and thiourea (0.3 g) were added in 30 ml of deionized water, and the mixture was vigorously stirred until it becomes transparent yellow. Then, hollow poly(aniline-co-pyrrole) spheres with SnO_2 (PACP/SnO_2) nanospheres were fabricated through one-step micelle-interfacial copolymerization in the presence of the above SnO_2 colloid. Sixty milliliters of aqueous solution containing 0.06 g of Triton X-100 and a certain amount of SnO_2 colloid was first prepared, and then pyrrole (0.38 ml, 0.09 M) and aniline (0.49 ml, 0.09 M) were added respectively. Subsequently, the suspension was subjected to stirring and ultrasonification for each 30 min, respectively, to obtain a homogeneous mixture. After cooling to 0°C for 30 min, a precooled aqueous solution of ammonium persulfate (2.47 g) dissolved in 5 ml of deionized water was added quickly to initiate polymerization under intensive stirring, and then the reaction proceeded for 12 hours without agitation at 0°C. The product was collected by filtration and dried in an oven at 60°C, yielding PACP/SnO_2. The resulting At-Sn@HCN was obtained by carbonization at 700°C for 3 hours with a heating rate of 5°C min^{-1} under N_2 atmosphere, in which the amount of SnO_2 colloid is 5.5 mM (2.5 ml). For comparison, Ex-Sn/HCN was prepared under similar conditions except that the amount of SnO_2 colloid was set to be 22 mM (10 ml). Commercial SnO_2 particles were also used instead of SnO_2 colloid for comparison. HCN was prepared similarly via the micelle-interfacial copolymerization. At-Sn@HCN etching was prepared by immersing At-Sn@HCN into excess hydrochloric acid (1 M) with stirring overnight, followed by washing and drying.

Materials characterization

The morphology and microstructure were characterized through field-emission SEM (NANOSEM450, FEI) and TEM (Talos F200X, FEI). Particle size distribution was obtained by statistical analysis of about 100 spheres at random from SEM images. The X-ray

diffractometer (MAXima_X XRD-7000) was used for detecting the presence of Sn particles and for the formation of amorphous carbons. The content of Sn was measured by TG analysis (METTLER TOLEDO). The N_2 adsorption-desorption measurements were conducted using an automated gas sorption analyzer (Micromeritics ASAP 2460) at 77 K, and the calculation of Brunauer-Emmett-Teller (BET) surface area was based on BET theory. XANES measurements for the Sn K-edge of At-Sn@HCN and Sn foil were conducted in transmission mode (fluorescence mode) on beamline 12-BM in the Advanced Photon Source at Argonne National Laboratory, while the XANES of electrodes of At-Sn@HCN and Sn microparticles after sodiation (discharge to 0.01 V) were measured on the BL14W1 beamline of Shanghai Synchrotron Radiation Facility. The X-ray photoelectron spectroscopy (Shimadzu Kratos Axis Supra) was used for analyzing the doped N in carbons.

Electrochemical measurement

Na stripping/plating in the electrodes were measured in a CR2025 coin-type test cell with an electrolyte of 1 M $NaPF_6$ in diglyme (35 μl in each cell) for half- and symmetric cells. The working electrode (substrate for Na plating/stripping) was prepared by mixing the active materials (e.g., At-Sn@HCN, HCN, or Ex-Sn/HCN) and the binder (carboxymethylcellulose sodium:styrene-butadiene rubber = 4:1 in mass ratio) in a weight ratio of 23:3 using water as the dispersant on Cu foil (12 mm in diameter), and the mass loading of the nucleation buffer layer is 1 to 1.2 mg cm^{-2}.

The half-cell was assembled using the above electrode (or bare Cu foil) and a metallic Na foil (10 mm in diameter) as the working and counter electrode, respectively, and the separator is Celgard 2500. Before testing, the half-cells were activated for 5 cycles between 0.01 and 1 V (versus Na^+/Na) under 0.1 mA cm^{-2}. The CE was assessed by the ratio of Na stripping capacity to Na plating capacity, in which a fixed capacity was first electrochemically plated under constant current density and then stripped away with a fixed potential. Unless otherwise stated, the cutoff stripping potential is set to 1 V.

For the configuration of the symmetric cell, two identical electrodes were prepared as follows: The Cu foil with the nucleation buffer layer electrode was first plated with a certain amount of Na at a current density of 1 mA cm^{-2} in half-cells, which were then disassembled to obtain the predeposited Na loading electrode (denoted as At-Sn@HCN/Na or HCN/Na). The symmetric cells were then assembled with the above identical predeposited Na electrodes (e.g., At-Sn@HCN/Na) for the plating/stripping measurement. The predeposition of Na loading is fixed at 4 mAh cm^{-2} for symmetrical cells with a plating/stripping capacity of 1 and 3.4 mAh cm^{-2}, whereas it is fixed at 10 mAh cm^{-2} with a plating/stripping capacity of 5 and 8 mAh cm^{-2}. The interfacial stability and voltage hysteresis were measured at different plating/stripping areal capacities under various current densities. CV was conducted on the CHI660 electrochemical workstation (Shanghai Chenhua). EIS measurements were conducted with a frequency range from 100 kHz to 100 mHz with an amplitude voltage of 10 mV using a Biologic Science Instrument (Bio-Logic SAS) with the symmetric cells.

For the full cell test, the cathode material is NVP, which was mixed with polyvinylidene fluoride and Super P with a weight ratio of 8:1:1 in *N*-methyl-2-pyrrolidone solvent. The slurry was coated onto the Al foil and dried in a vacuum oven at 60°C for 8 hours. The mass loading of NVP was around 3 mg cm^{-2} (0.35 mAh cm^{-2}), and high loading amount was controlled around 7 mg cm^{-2} (0.82 mAh cm^{-2}). The Sn@HCN/Na||NVP full cells were assembled with the NVP cathode and At-Sn@HCN/Na anode, whereas the full cell with Na predeposited on the bare Cu foil anode serves as control. The glass fiber membrane is used as a separator, and the electrolyte amount is 120 μl. The full cell was tested on a CT2001A battery test system (LAND, Wuhan LAND Electronic Co. Ltd., China) in the voltage range of 2.5 to 3.8 V.

DFT calculations

The DMol3 quantum mechanics program based on DFT is used for geometry optimization. The vacuum layer is 15 Å for Sn and $Na_{15}Sn_4$ crystals and 20 Å for graphene substrates, respectively, to avoid the interaction between adjacent layers. The Perdew-Burke-Ernzerhof function in general gradient approximation is chosen for exchange correlation energy. DFT semicore pseudo potential and double numerical plus polarization function are used considering the relativistic effect. The parameters of convergence for geometry optimization are demonstrated as follows: 1.0×10^{-5} Ha per atom for energy, 0.002 Ha $Å^{-1}$ for force, and 0.005 Å for displacement. The Monkhorst-Pack k-point sampling was $1 \times 1 \times 1$ for supercells of carbon (5×5) and $Na_{15}Sn_4$ (1×1) and $1 \times 2 \times 1$ for the Sn supercell (2×3). The adsorption energy (E_{ad}) is defined as $E_{ad} = E_{slab + Na} - E_{slab} - E_{Na}$, where $E_{slab + Na}$, E_{slab}, and E_{Na} refer to the energy of the total system, adsorption substrate, and Na atom, respectively. The calculation for differential charge density is from Cambridge Sequential Total Energy Package based on DFT. The self-consistent convergence condition is that the energy variation of a single atom is less than 1.0×10^{-6} eV.

SUPPLEMENTARY MATERIALS

Supplementary material for this article is available at https://science.org/doi/10.1126/sciadv.abm7489

REFERENCES AND NOTES

1. R. Usiskin, Y. X. Lu, J. Popovic, M. Law, P. Balaya, Y. S. Hu, J. Maier, Fundamentals, status and promise of sodium-based batteries. *Nat. Rev. Mater.* **6**, 1020–1035 (2021).
2. J. X. Zheng, Q. Zhao, T. Tang, J. F. Yin, C. D. Quilty, G. D. Renderos, X. T. Liu, Y. Deng, L. Wang, D. C. Bock, C. Jaye, D. H. Zhang, E. S. Takeuchi, K. J. Takeuchi, A. C. Marschilok, L. A. Archer, Reversible epitaxial electrodeposition of metals in battery anodes. *Science* **366**, 645–648 (2019).
3. C. X. Chu, R. Li, F. P. Cai, Z. C. Bai, Y. X. Wang, X. Xu, N. N. Wang, J. Yang, S. X. Dou, Recent advanced skeletons in sodium metal anodes. *Energy Environ. Sci.* **14**, 4318–4340 (2021).
4. B. Lee, E. Paek, D. Mitlin, S. W. Lee, Sodium metal anodes: Emerging solutions to dendrite growth. *Chem. Rev.* **119**, 5416–5460 (2019).
5. Z. W. Seh, J. Sun, Y. M. Sun, Y. Cui, A highly reversible room-temperature sodium metal anode. *ACS Cent. Sci.* **1**, 449–455 (2015).
6. K. Doi, Y. Yamada, M. Okoshi, J. Ono, C. P. Chou, H. Nakai, A. Yamada, Reversible sodium metal electrodes: Is fluorine an essential interphasial component? *Angew. Chem. Int. Ed.* **58**, 8024–8028 (2019).
7. P. C. Wen, P. F. Lu, X. Y. Shi, Y. Yao, H. Shi, H. Q. Liu, Y. Yu, Z.-S. Wu, Photopolymerized gel electrolyte with unprecedented room-temperature ionic conductivity for high-energy-density solid-state sodium metal batteries. *Adv. Energy Mater.* **11**, 2002930 (2021).
8. Y. M. Chen, Z. Q. Wang, X. Y. Li, X. H. Yao, C. Wang, Y. T. Li, W. J. Xue, D. W. Yu, S. Y. Kim, F. Yang, A. Kushima, G. G. Zhang, H. T. Huang, N. Wu, Y. W. Mai, J. B. Goodenough, J. Li, Li metal deposition and stripping in a solid-state battery via Coble creep. *Nature* **578**, 251–255 (2020).
9. Y. Zhao, L. V. Goncharova, Q. Zhang, P. Kaghazchi, Q. Sun, A. Lushington, B. Q. Wang, R. Y. Li, X. L. Sun, Inorganic-organic coating via molecular layer deposition enables long life sodium metal anode. *Nano Lett.* **17**, 5653–5659 (2017).
10. M. Zhu, G. Y. Wang, X. Liu, B. K. Guo, G. Xu, Z. Y. Huang, M. H. Wu, H. K. Liu, S. X. Dou, C. Wu, Dendrite-free sodium metal anodes enabled by a sodium benzenedithiolate-rich protection layer. *Angew. Chem. Int. Ed.* **59**, 6596–6600 (2020).
11. Y. Zhao, L. V. Goncharova, A. Lushington, Q. Sun, H. Yadegari, B. Q. Wang, W. Xiao, R. Y. Li, X. L. Sun, Superior stable and long life sodium metal anodes achieved by atomic layer deposition. *Adv. Mater.* **29**, 1606663 (2017).

12. Z. P. Li, K. J. Zhu, P. Liu, L. F. Jiao, 3D confinement strategy for dendrite-free sodium metal batteries. *Adv. Energy Mater.* **12**, 2100359 (2022).
13. L. Ye, M. Liao, T. C. Zhao, H. Sun, Y. Zhao, X. M. Sun, B. J. Wang, H. S. Peng, A sodiophilic interphase-mediated, dendrite-free anode with ultrahigh specific capacity for sodium-metal batteries. *Angew. Chem. Int. Ed.* **58**, 17054–17060 (2019).
14. T. Li, J. Sun, S. Gao, B. Xiao, J. Cheng, Y. Zhou, X. Sun, F. Jiang, Z. Yan, S. Xiong, Superior sodium metal anodes enabled by sodiophilic carbonized coconut framework with 3D tubular structure. *Adv. Energy Mater.* **11**, 2003699 (2021).
15. C. X. Chu, N. N. Wang, L. L. Li, L. D. Lin, F. Tian, Y. L. Li, J. Yang, S. X. Dou, Y. T. Qian, Uniform nucleation of sodium in 3D carbon nanotube framework via oxygen doping for long-life and efficient Na metal anodes. *Energy Storage Mater.* **23**, 137–143 (2019).
16. Y. Xu, C. L. Wang, E. Matios, J. M. Luo, X. F. Hu, Q. Yue, Y. J. Kang, W. Y. Li, Sodium deposition with a controlled location and orientation for dendrite-free sodium metal batteries. *Adv. Energy Mater.* **10**, 2002308 (2020).
17. N. H. Zhu, X. G. Mao, G. Y. Wang, M. Zhu, H. Y. Wang, G. Xu, M. H. Wu, H. K. Liu, S. X. Dou, C. Wu, Stable sodium metal anodes with a high utilization enabled by an interfacial layer composed of yolk-shell nanoparticles. *J. Mater. Chem. A* **9**, 13200–13208 (2021).
18. G. Y. Wang, F. F. Yu, Y. Zhang, Y. J. Zhang, M. Zhu, G. Xu, M. H. Wu, H. K. Liu, S. X. Dou, C. Wu, 2D Sn/C freestanding frameworks as a robust nucleation layer for highly stable sodium metal anodes with a high utilization. *Nano Energy* **79**, 105457 (2021).
19. W. Liu, Z. D. Chen, Z. Zhang, P. X. Jiang, Y. G. Chen, E. Paek, Y. X. Wang, D. Mitlin, Lithium-activated SnS-graphene alternating nanolayers enable dendrite-free cycling of thin sodium metal anodes in carbonate electrolyte. *Energy Environ. Sci.* **14**, 382–395 (2021).
20. X. Y. Zheng, P. Li, Z. Cao, W. Luo, F. Z. Sun, Z. Q. Wang, B. Ding, G. X. Wang, Y. H. Huang, Boosting the reversibility of sodium metal anode via heteroatom-doped hollow carbon fibers. *Small* **15**, 1902688 (2019).
21. Z. J. Zheng, X. X. Zeng, H. Ye, F. F. Cao, Z. B. Wang, Nitrogen and oxygen co-doped graphitized carbon fibers with sodiophilic-rich sites guide uniform sodium nucleation for ultrahigh-capacity sodium-metal anodes. *ACS Appl. Mater. Interfaces* **10**, 30417–30425 (2018).
22. B. Sun, P. Li, J. Q. Zhang, D. Wang, P. Munroe, C. Y. Wang, P. H. L. Notten, G. X. Wang, Dendrite-free sodium-metal anodes for high-energy sodium-metal batteries. *Adv. Mater.* **30**, 1801334 (2018).
23. J. X. Wu, P. C. Zou, M. Ihsan-Ul-Haq, N. Mubarak, A. Susca, B. H. Li, F. Ciucci, J. K. Kim, Sodiophilically graded gold coating on carbon skeletons for highly stable sodium metal anodes. *Small* **16**, 2003815 (2020).
24. S. Tang, Y. Y. Zhang, X. G. Zhang, J. T. Li, X. Y. Wang, J. W. Yan, D. Y. Wu, M. S. Zheng, Q. F. Dong, B. W. Mao, Stable Na plating and stripping electrochemistry promoted by in situ construction of an alloy-based sodiophilic interphase. *Adv. Mater.* **31**, 1807495 (2019).
25. M. Q. Zhu, S. M. Li, B. Li, Y. J. Gong, Z. G. Du, S. B. Yang, Homogeneous guiding deposition of sodium through main group II metals toward dendrite-free sodium anodes. *Sci. Adv.* **5**, eaau6264 (2019).
26. T. Z. Yang, T. Qian, Y. W. Sun, J. Zhong, F. Rosei, C. L. Yan, Mega high utilization of sodium metal anodes enabled by single zinc atom sites. *Nano Lett.* **19**, 7827–7835 (2019).
27. H. Wang, E. Matios, C. L. Wang, J. M. Luo, X. Lu, X. F. Hu, Y. W. Zhang, W. Y. Li, Tin nanoparticles embedded in a carbon buffer layer as preferential nucleation sites for stable sodium metal anodes. *J. Mater. Chem. A* **7**, 23747–23755 (2019).
28. G. Y. Wang, Y. Zhang, B. K. Guo, L. Tang, G. Xu, Y. J. Zhang, M. H. Wu, H. K. Liu, S. X. Dou, C. Wu, Core-shell C@Sb nanoparticles as a nucleation layer for high-performance sodium metal anodes. *Nano Lett.* **20**, 4464–4471 (2020).
29. L. Zhang, X. L. Zhu, G. Y. Wang, G. Xu, M. H. Wu, H. K. Liu, S. X. Dou, C. Wu, Bi nanoparticles embedded in 2D carbon nanosheets as an interfacial layer for advanced sodium metal anodes. *Small* **17**, 2007578 (2021).
30. J. M. Luo, C. L. Wang, H. Wang, X. F. Hu, E. Matios, X. Lu, W. K. Zhang, X. Y. Tao, W. Y. Li, Pillared MXene with ultralarge interlayer spacing as a stable matrix for high performance sodium metal anodes. *Adv. Funct. Mater.* **29**, 1805946 (2019).
31. Q. L. Chen, B. Liu, L. Zhang, Q. S. Xie, Y. G. Zhang, J. Lin, B. H. Qu, L. S. Wang, B. S. Sa, D. L. Peng, Sodiophilic Zn/SnO_2 porous scaffold to stabilize sodium deposition for sodium metal batteries. *Chem. Eng. J.* **404**, 126469 (2021).
32. J. M. Luo, X. Lu, E. Matios, C. L. Wang, H. Wang, Y. W. Zhang, X. F. Hu, W. Y. Li, Tunable MXene-derived 1D/2D hybrid nanoarchitectures as a stable matrix for dendrite-free and ultrahigh capacity sodium metal anode. *Nano Lett.* **20**, 7700–7708 (2020).
33. K. Yan, Z. D. Lu, H. W. Lee, F. Xiong, P. C. Hsu, Y. Z. Li, J. Zhao, S. Chu, Y. Cui, Selective deposition and stable encapsulation of lithium through heterogeneous seeded growth. *Nat. Energy* **1**, 16010 (2016).
34. R. Xu, X. B. Cheng, C. Yan, X. Q. Zhang, Y. Xiao, C. Z. Zhao, J. Q. Huang, Q. Zhang, Artificial interphases for highly stable lithium metal anode. *Matter* **1**, 317–344 (2019).
35. M. S. Kim, Deepika, S. H. Lee, M. S. Kim, J. H. Ryu, K. R. Lee, L. A. Archer, W. I. Cho, Enabling reversible redox reactions in electrochemical cells using protected LiAl intermetallics as lithium metal anodes. *Sci. Adv.* **5**, eaax5587 (2019).
36. J. C. Sun, M. Zhang, P. Ju, Y. Hu, X. X. Chen, W. R. Z. Wang, C. C. Chen, Long-life sodium metal anodes achieved by cuprous oxide-modified Ni foam host. *Energ. Technol.* **8**, 1901250 (2020).
37. Y. Zhong, Q. Shi, C. Zhu, Y. Zhang, M. Li, J. S. Francisco, H. Wang, Mechanistic insights into fast charging and discharging of the sodium metal battery anode: A comparison with lithium. *J. Am. Chem. Soc.* **143**, 13929–13936 (2021).
38. Z. Y. Zhang, X. X. Zhao, S. B. Xi, L. L. Zhang, Z. X. Chen, Z. P. Zeng, M. Huang, H. B. Yang, B. Liu, S. J. Pennycook, P. Chen, Atomically dispersed cobalt trifunctional electrocatalysts with tailored coordination environment for flexible rechargeable Zn-air battery and self-driven water splitting. *Adv. Energy Mater.* **10**, 2002896 (2020).
39. X. Y. Lu, S. S. Gao, H. Lin, L. D. Yu, Y. H. Han, P. A. Zhu, W. C. Bao, H. L. Yao, Y. Chen, J. L. Shi, Bioinspired copper single-atom catalysts for tumor parallel catalytic therapy. *Adv. Mater.* **32**, 2002246 (2020).
40. L. N. Song, W. Zhang, Y. Wang, X. Ge, L. C. Zou, H. F. Wang, X. X. Wang, Q. C. Liu, F. Li, J. J. Xu, Tuning lithium-peroxide formation and decomposition routes with single-atom catalysts for lithium-oxygen batteries. *Nat. Commun.* **11**, 2191 (2020).
41. Y. Pan, R. Lin, Y. J. Chen, S. J. Liu, W. Zhu, X. Cao, W. X. Chen, K. L. Wu, W. C. Cheong, Y. Wang, L. R. Zheng, J. Luo, Y. Lin, Y. Q. Liu, C. G. Liu, J. Li, Q. Lu, X. Chen, D. S. Wang, Q. Peng, C. Chen, Y. D. Li, Design of single-atom Co–N_5 catalytic site: A robust electrocatalyst for CO_2 reduction with nearly 100% CO selectivity and remarkable stability. *J. Am. Chem. Soc.* **140**, 4218–4221 (2018).
42. F. Xu, Z. W. Tang, S. Q. Huang, L. Y. Chen, Y. R. Liang, W. C. Mai, H. Zhong, R. W. Fu, D. C. Wu, Facile synthesis of ultrahigh-surface-area hollow carbon nanospheres for enhanced adsorption and energy storage. *Nat. Commun.* **6**, 7221 (2015).
43. F. Xu, Y. H. Lu, J. H. Ma, Z. K. Huang, Q. F. Su, R. W. Fu, D. C. Wu, Facile, general and template-free construction of monodisperse yolk–shell metal@carbon nanospheres. *Chem. Commun.* **53**, 12136–12139 (2017).
44. F. Xu, B. C. Ding, Y. Q. Qiu, R. H. Dong, W. Q. Zhuang, X. S. Xu, H. J. Han, J. Y. Yang, B. Q. Wei, H. Q. Wang, S. Kaskel, Generalized domino-driven synthesis of hollow hybrid carbon spheres with ultrafine metal nitrides/oxides. *Matter* **3**, 246–260 (2020).
45. Y. F. Chen, Z. J. Li, Y. B. Zhu, D. M. Sun, X. E. Liu, L. Xu, Y. W. Tang, Atomic Fe dispersed on N-doped carbon hollow nanospheres for high-efficiency electrocatalytic oxygen reduction. *Adv. Mater.* **31**, 1806312 (2019).
46. B. Zheng, X. Lin, X. Zhang, D. Wu, K. Matyjaszewski, Emerging functional porous polymeric and carbonaceous materials for environmental treatment and energy storage. *Adv. Funct. Mater.* **30**, 1907006 (2019).
47. W. H. Lai, H. Wang, L. R. Zheng, Q. Jiang, Z. C. Yan, L. Wang, H. Yoshikawa, D. Matsumura, Q. Sun, Y. X. Wang, Q. F. Gu, J. Z. Wang, H. K. Liu, S. L. Chou, S. X. Dou, General synthesis of single-atom catalysts for hydrogen evolution reactions and room-temperature Na-S batteries. *Angew. Chem. Int. Ed.* **59**, 22171–22178 (2020).
48. J. Wu, F. Xu, S. Li, P. Ma, X. Zhang, Q. Liu, R. Fu, D. Wu, Porous polymers as multifunctional material platforms toward task-specific applications. *Adv. Mater.* **31**, 1802922 (2019).
49. X. He, S. Jin, L. C. Miao, Y. C. Cai, Y. P. Hou, H. X. Li, K. Zhang, Z. H. Yan, J. Chen, A 3D hydroxylated MXene/carbon nanotubes composite as a scaffold for dendrite-free sodium-metal electrodes. *Angew. Chem. Int. Ed.* **59**, 16705–16711 (2020).
50. F. Wu, J. H. Zhou, R. Luo, Y. X. Huang, Y. Mei, M. Xie, R. J. Chen, Reduced graphene oxide aerogel as stable host for dendrite-free sodium metal anode. *Energy Storage Mater.* **22**, 376–383 (2019).
51. A. X. Wang, X. F. Hu, H. Q. Tang, C. Y. Zhang, S. Liu, Y. W. Yang, Q. H. Yang, J. Y. Luo, Processable and moldable sodium-metal anodes. *Angew. Chem. Int. Ed.* **56**, 11921–11926 (2017).
52. H. Ye, C. Y. Wang, T. T. Zuo, P. F. Wang, Y. X. Yin, Z. J. Zheng, P. Wang, J. Cheng, F. F. Cao, Y. G. Guo, Realizing a highly stable sodium battery with dendrite-free sodium metal composite anodes and O3-type cathodes. *Nano Energy* **48**, 369–376 (2018).
53. L. Wang, J. Shang, Q. Huang, H. Hu, Y. Zhang, C. Xie, Y. Luo, Y. Gao, H. Wang, Z. Zheng, Smoothing the sodium-metal anode with a self-regulating alloy interface for high-energy and sustainable sodium-metal batteries. *Adv. Mater.* **33**, 2102802 (2021).
54. Y. Xie, J. Hu, Z. Han, T. Wang, J. Zheng, L. Gan, Y. Lai, Z. Zhang, Encapsulating sodium deposition into carbon rhombic dodecahedron guided by sodiophilic sites for dendrite-free Na metal batteries. *Energy Storage Mater.* **30**, 1–8 (2020).
55. M. Guo, H. L. Dou, W. Y. Zhao, X. L. Zhao, B. X. Wan, J. H. Wang, Y. T. Yan, X. M. Wang, Z. F. Ma, X. W. Yang, Three dimensional frameworks of super ionic conductor for thermodynamically and dynamically favorable sodium metal anode. *Nano Energy* **70**, 104479 (2020).
56. P. Y. Kuang, Y. R. Wang, B. C. Zhu, F. J. Xia, C. W. Tung, J. S. Wu, H. M. Chen, J. G. Yu, Pt single atoms supported on N-doped mesoporous hollow carbon spheres with enhanced electrocatalytic H_2-evolution activity. *Adv. Mater.* **33**, 2008599 (2021).
57. M. Zhou, Y. Jiang, G. Wang, W. J. Wu, W. X. Chen, P. Yu, Y. Q. Lin, J. J. Mao, L. Q. Mao, Single-atom Ni-N_4 provides a robust cellular NO sensor. *Nat. Commun.* **11**, 3188 (2020).

58. Q. C. Feng, S. Zhao, Q. Xu, W. X. Chen, S. B. Tian, Y. Wang, W. S. Yan, J. Luo, D. S. Wang, Y. D. Li, Mesoporous nitrogen-doped carbon-nanosphere-supported isolated single-atom Pd catalyst for highly efficient semihydrogenation of acetylene. *Adv. Mater.* **31**, 1901024 (2019).
59. H. B. Zhang, Y. Y. Liu, T. Chen, J. T. Zhang, J. Zhang, X. W. Lou, Unveiling the activity origin of electrocatalytic oxygen evolution over isolated Ni atoms supported on a N-doped carbon matrix. *Adv. Mater.* **31**, 1904548 (2019).
60. Y. H. Han, Y. G. Wang, W. X. Chen, R. R. Xu, L. R. Zheng, J. Zhang, J. Luo, R. A. Shen, Y. Q. Zhu, W. C. Cheong, C. Chen, Q. Peng, D. S. Wang, Y. D. Li, Hollow N-doped carbon spheres with isolated cobalt single atomic sites: Superior electrocatalysts for oxygen reduction. *J. Am. Chem. Soc.* **139**, 17269–17272 (2017).
61. W. Yang, W. Yang, L. B. Dong, G. J. Shao, G. X. Wang, X. W. Peng, Hierarchical ZnO nanorod arrays grown on copper foam as an advanced three-dimensional skeleton for dendrite-free sodium metal anodes. *Nano Energy* **80**, 105563 (2021).
62. S. S. Chi, X. G. Qi, Y. S. Hu, L. Z. Fan, 3D flexible carbon felt host for highly stable sodium metal anodes. *Adv. Energy Mater.* **8**, 1702764 (2018).
63. X. Y. Cui, Y. J. Wang, H. D. Wu, X. D. Lin, S. Tang, P. Xu, H. G. Liao, M. S. Zheng, Q. F. Dong, A carbon foam with sodiophilic surface for highly reversible, ultra-long cycle sodium metal anode. *Adv. Sci.* **8**, 2003178 (2021).

Acknowledgments: We appreciate J. Ma (BL14W1 beamline of Shanghai Synchrotron Radiation Facility) for help in XANES test of samples after sodiation, and we would like to thank the Analytical & Testing Center of Northwestern Polytechnical University for XPS and TEM characterizations.

Funding: Xingcai Zhang and Jiashen Meng acknowledge the support from Harvard/MIT. Other authors acknowledge the support of the project of NSFC (51972270 to F.X.), the project of National Key R&D Program for International Cooperation (2021YFE0115100 to H.W.), the Natural Science Foundation of Shaanxi Province (2020JZ-07 to F.X.), the Key Research and Development Program of Shaanxi Province (2019TSLGY07-03 to F.X. and 2021ZDLGY14-08 to H.W.), the Fundamental Research Funds for the Central Universities (3102019JC005 to H.W.), the Research Fund of the State Key Laboratory of Solidification Processing (NPU), China (2021-TS-03 to F.X.), and the Research Fund of the State Key Laboratory of Solid Lubrication (CAS), China (LSL-2007 to F.X.). **Author contributions:** Xingcai Zhang, F.X., L.L., and H.W. conceived the concept and directed the research. C.Q. and B.D. carried out the synthesis and characterization of HCN and its Sn composites with the help of Y.Q. and J.Y. C.Q. assembled the cell for Na metal anode and performed the electrochemical performance with the guide of Q.L. X.X. performed the TEM and HAADF-STEM characterization. Xiuhai Zhang performed DFT calculations. Jingyuan Ma and G.J. carried out EXAFS test, and P.Y. assisted in the analysis of XANES and EXAFS results. S.K., Jiashen Meng, and F.C. gave advice to the research. Xingcai Zhang, F.X., and C.Q. wrote the manuscript. **Competing interests:** The authors declare that they have no competing interests. **Data and materials availability:** All data needed to evaluate the conclusions in the paper are present in the paper and/or the Supplementary Materials.

Submitted 8 October 2021
Accepted 24 March 2022
Published 11 May 2022
10.1126/sciadv.abm7489

ScienceAdvances

Atomic Sn–enabled high-utilization, large-capacity, and long-life Na anode

Fei XuChangzhen QuQiongqiong LuJiashen MengXiuhai ZhangXiaosa XuYuqian QiuBaichuan DingJiaying YangFengren CaoPenghui YangGuangshen JiangStefan KaskelJingyuan MaLiang LiXingcai ZhangHongqiang Wang

Sci. Adv., 8 (19), eabm7489. • DOI: 10.1126/sciadv.abm7489

Science Advances (ISSN) is published by the American Association for the Advancement of Science. 1200 New York Avenue NW, Washington, DC 20005. The title *Science Advances* is a registered trademark of AAAS.